Supporting Information

Giant Exciton Transport in hBN/2D-Perovskite Heterostructures

Sara Darbari[1,2,†*], Paul Bittorf[1,†], Leon Multerer[1], Fatemeh Chahshouri[1], Parsa Darman[1,2], Pavel Ruchka[3], Harald Giessen[3], Masoud Taleb[1,4], Yaser Abdi[1,5], Nahid Talebi[1,4*]

[1]Institute of Experimental and Applied Physics, Kiel University, 24418 Kiel, Germany

[2]Faculty of Electrical and Computer Engineering, Tarbiat Modares University, Tehran 1411713116, Iran

[3]4[th] Physics Institute and Research Center SCoPE, University of Stuttgart, 70569 Stuttgart, Germany

[4]Kiel Nano, Surface, and Interface Science KiNSIS, Kiel University, 24118 Kiel, Germany

[5]Physics Department, University of Tehran, Tehran 1439955961, Iran

† These authors contributed equally to this work.

Corresponding Authors:

**Email*: talebi@physik.uni-kiel.de (N. T.).

**Email*: s.darbari@modares.ac.ir (S. D.).

Supplementary Note 1: Exploring the electron-beam-induced degradation effect

To investigate the suitable conditions for CL measurements on RPP-based samples, we utilize two approaches: (i) hBN-encapsulation, and (ii) finding appropriate electron beam conditions to achieve an efficient exciton excitation and avoiding the degradation issue.

To evaluate the protection functionality of the hBN layer against electron beam irradiation, RPP flakes that are partially covered by a large hBN flake (Supplementary Figure 1a) are exposed to an intense electron beam condition at high sample current of 16 nA and acceleration voltage of 10 kV in the scanning electron microscope (SEM). The uncovered part of RPP flakes show a drastic electron beam induced degradation, while the covered part is protected (Supplementary Figure 1b). Therefore, the realized hBN/RPP heterostructure surpasses the electron beam induced degradation in CL measurements.

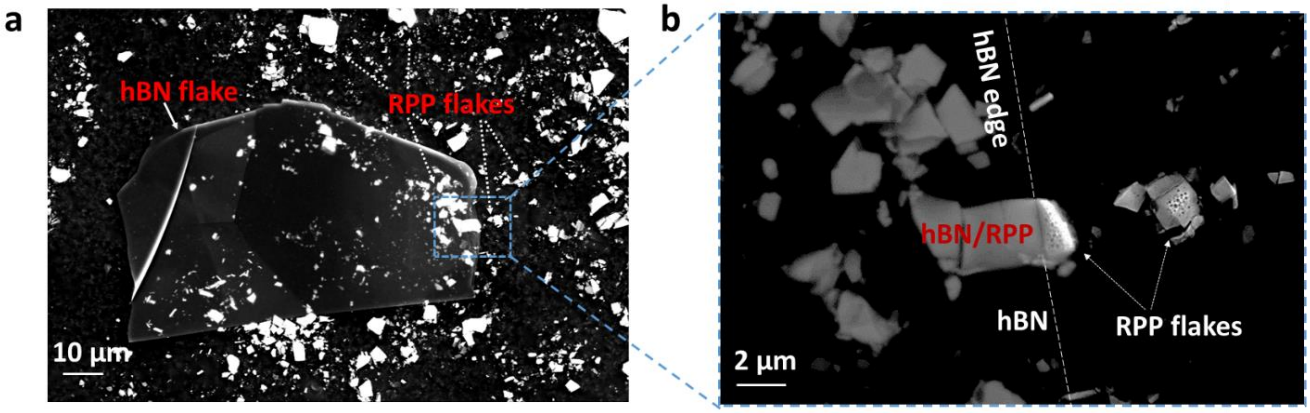

Supplementary Figure 1: Protection efficiency of hBN encapsulation of RPP flakes against an intense electron beam condition, at a high current of 16 nA, acceleration voltage of 10 kV and acquisition time of 500 ms in the SEM apparatus. (a) Secondary-electron SEM image of a large hBN flake exfoliated on multiple RPP flakes. (b)The magnified view of the partially covered RPP flake at the edge of hBN flake. Uncovered parts of RPP flakes (right side) are drastically degraded, while encapsulation by hBN flake has significantly hindered the electron-beam induced degradation.

To investigate the efficiency of exciton excitation yield by electron beam in unencapsulated RPP flakes, while keeping a low degradation rate, we change the acceleration voltage (10 kV, 15 kV and 20 kV in Supplementary Figure 2) at a fixed low current of 200 pA in the mirror-collected CL spectroscopy. Efficient excitation of bulk excitons along the scanning length by the electron beam (shown by blue arrows) is confirmed for acceleration voltage of 20 kV (Supplementary Figure 2a), as opposed to lower acceleration voltages that lead to excitation of excitons merely at the flake edge (Supplementary Figure 2b and 2d). Moreover, Supplementary Figure 2 does not show any detectable degradation trace either in the secondary electron images of RPP flakes, nor in the CL peak intensity when using low electron currents. Hence, we fix the acceleration voltage at 20 kV and the electron beam current below 200 pA, where the current is measured at the sample position, to investigate RPPs and the hBN/RPP heterostructures.

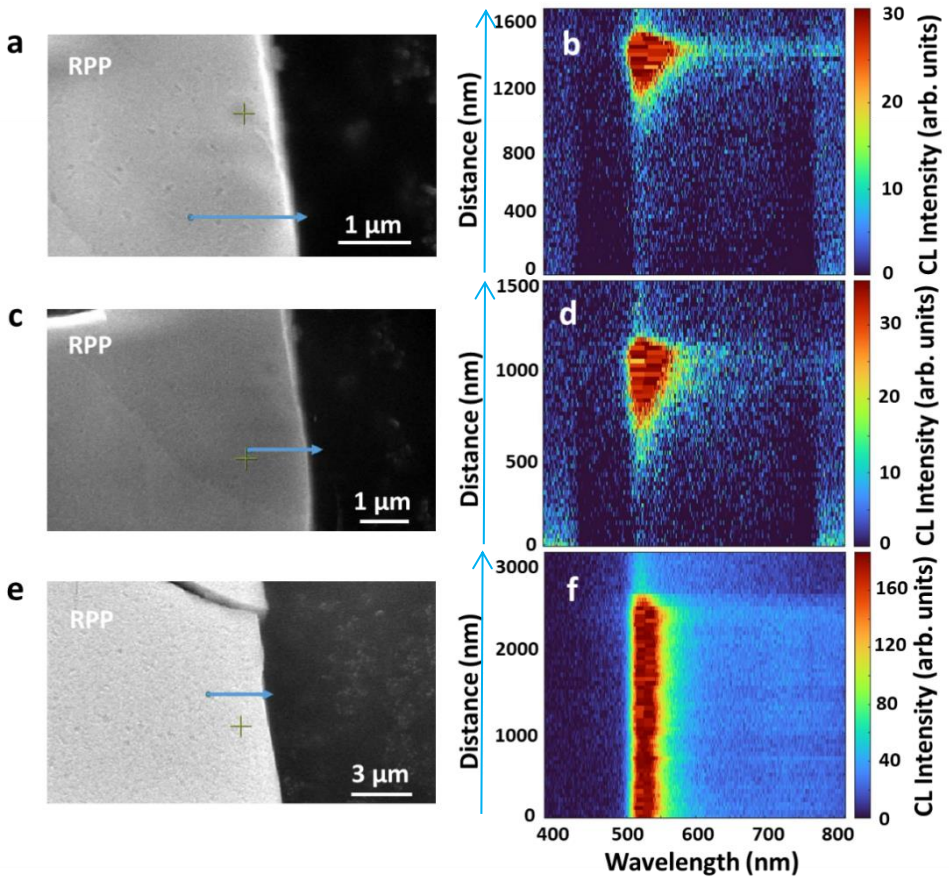

Supplementary Figure 2: Exciton excitation efficiency of the unencapsulated RPP flakes at different acceleration voltages explored by the mirror-collected CL spectroscopy. Scanning the electron beam along the blue arrows shown in the left images in parts (a, c, e). Current level is fixed at 200 pA for all measurements to avoid the electron beam induced degradation in RPP. The measured CL spectra along the scanning length at acceleration voltages of (b) 10 kV, (d) 15 kV, and (f) 20 kV. Acceleration voltages below 20 kV leads to exciton excitation just at flake edges, while (f) proves efficient excitation of bulk excitons in RPP flakes without considerable degradation.

Supplementary Note 2: Calculating the Coupling Coefficients g_{ed}

The interaction between excitons and defects is exclusive to the RPP/hBN heterostructures. Once an exciton is excited by the electron beam, it transitions to the defect state through phonon interactions. This process is notably efficient as the defects in the hBN flake have resonant wavelengths that are nearly identical to the exciton, differing by only 5 nm. Subsequently, these excitons are accommodated by these defects resonating at 530 nm, enabling the excitons to travel significant distances. The excitons are hosted by these defects and subsequently interact with the more abundantly occurring defects, resonating at the wavelength of 800 nm, via Coulomb interactions. Therefore, the hopping of the excitons up to long distances is mediated by the Coulomb interactions between the first and second defects that are modeled by the Hamiltonian

$\hat{H}_C = \frac{1}{2} V_{\text{ed}}\, a_2^{e\dagger} a_1^{d\dagger} a_2^{d} a_1^{e}$, where V_{ed} is the coulomb coupling strength, $a_2^{e\dagger}$ and a_1^{e} are the creation and annihilation operators associated with the two-level systems of the defects, resonating at 530 nm, correspondingly. $a_1^{d\dagger}$ and a_2^{d} are also the creation and annihilation operators for the other defect two-level system. The subscript numbers specify the states, 1 associated with the initial and 2 with the excited states. The g_{ed} coupling strength is obtained as

$$g_{\text{ed}} = \frac{V_{ed}}{\hbar} = \frac{e^2}{4\pi\hbar\varepsilon_0\varepsilon_r} \int d^3x \int d^3x' \psi_2^{e*}(x) \psi_1^{d*}(x') \frac{1}{|x - x'|} \psi_2^{d}(x') \psi_1^{e}(x), \quad (1)$$

where ψ_i^e, ψ_i^d are the wave functions associated with the i^{th} states of the exciton and defect quantum systems. We model the exciton and defect quantum systems by displaced harmonic oscillators with the resonant wavelengths of 530 nm and 800 nm, respectively, between their ground and first excited quantum states. Considering a random displacement between the centers of the wavefunctions of both defects ranging from 1 nm to 3 nm, we find out that the values for the coupling strength can change between 2 $(\text{ns})^{-1}$ to almost 0 value. An average value for the diffusion coefficient is $D = 3955\ \text{cm}^2 \cdot \text{s}^{-1}$ as pointed out in the main text.

Supplementary Note 3: Complementary Measurements to Confirm the Long-Range Exciton Transport in HBN/RPP Heterostructures

The optical properties of another RPP flake that was partially covered by a large hBN flake is studied here by utilizing the fiber-collected CL spectroscopy. First, we scan the sample by moving the electron beam excitation spot while keeping the position of the detecting fiber fixed (at the cross mark in Supplementary Figure 3a). Second, the detecting fiber is moved over the heterostructure, while keeping the electron excitation position fixed (at the cross mark in Supplementary Figure 3d). Thereby, we would be able to determine the effect of changing the excitation and detection positions in the investigated hBN/RPP heterostructure on the CL emission, in addition to probing the propagation characteristic of the excited excitons at the hBN/RPP heterostructure over long-range distances. In the first measurement, when the electron beam impacts the tapered-like edge of the unencapsulated RPP flake, edge excitons are efficiently excited, leading to a strong and broad CL peak (shown by orange zones and spectrum in Supplementary Figure 3(a-c)). However, when the electron beam impacts the surface of the unencapsulated RPP flake the excitonic peak intensity decreases and remains constant, until the electron beam impacts the hBN edge on top of RPP flake. Scanning to the hBN/RPP heterostructure by passing through the hBN edge (shown by red zones and spectrum in Supplementary Figure 3(a-c)), the excitonic peak increases in consistency with the luminescent enhancement in Fig. 1d and Fig. 2c, d. Next, passing over the underlying RPP edge and scanning on the extruded part of hBN (shown by black zones and spectrum in Supplementary Figure 3(a-c)) the excitonic peak intensity is decreased, but remains at a constant value. Scanning the electron beam over the wrinkles in the extruded hBN flake leads to a higher CL intensity at the excitonic peak, which can be attributed to exciting higher local defects density in hBN that improves the resonance response of the coupled

exciton-defect system. Moreover, the emergence of the narrowed, red-shifted CL spectra in exciting the hBN/RPP heterostructure (red peak), and the extruded part of hBN (black peak) are reconfirmed in Supplementary Figure 3(c).

In the second step of this measurement, by scanning the fiber away from the RPP edge, while continuously measuring the emitted CL spectra, we observe the excitonic peak at 535 nm on the extruded part of the hBN flake over a long distance up to 100 µm (Supplementary Figure 3(d, e)). Moreover, a higher excitonic CL intensity is collected at hBN wrinkles, which is related to higher portion of excitonic radiative decay at defects, discontinuities and edges (Supplementary Figure 3(e)). This measurement confirms a spatial exponentially decaying behavior of the excitonic peak intensity over the long range, wherein an exponential curve of with decaying coefficient of $\gamma =$ 154.9 µm is fitted to the average measured CL intensities (Supplementary Figure 3(f)), comparable with the measurement in Fig. 4d.

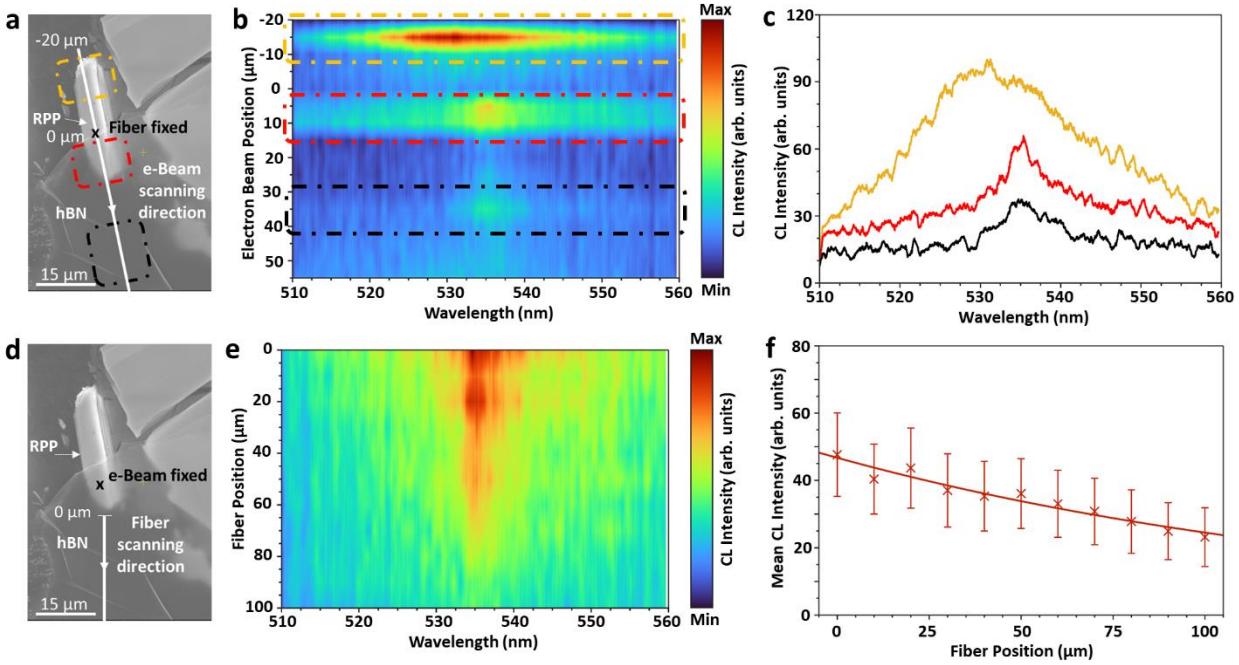

Supplementary Figure 3: Fiber-collected CL spectroscopy results of the hBN/RPP heterostructure. Secondary electron SEM image of the investigated RPP structure is demonstrated in both (a) and (d). (a) Fiber position is fixed on the sample at the cross mark, while electron beam is scanning the structure along the white arrow. (b) The measured CL spectra along the electron beam scanning path. The regions highlighted by the dash-dotted boxes correspond to the regions marked on the SEM image with the same colors. (c) CL spectra integrated over the selected regions specified by colored boxes in (b). (d) The electron beam position is fixed on the hBN/RPP heterostructure at the cross mark, while the fiber is scanning along the white arrow. (e) The measured CL spectra along the fiber's scanning path in part (c). (f) The mean excitonic peak intensity and standard deviation of the measured CL spectra from part (e) versus the scanning fiber position, fitted to an exponential function of exp(-x/γ) with a decaying coefficient of γ=154.9 µm.

Spatial decaying behavior of the excitonic CL peak has been also measured on a large pure RPP flake without any hBN flake. As illustrated in Supplementary Figure 4(a), electron beam has been fixed at the cross mark to excite RPP's excitons, and the CL-collecting fiber is scanning along the white arrow, up to 100 μm away from the excitation point. Supplementary Figure 4(b) exhibits the collected excitonic CL peak versus the fiber position, revealing the fast-decaying behavior of the peak intensity in pure RPP along a few micrometers, due to the secondary electrons excitations and the spatial resolution of the fiber collector.

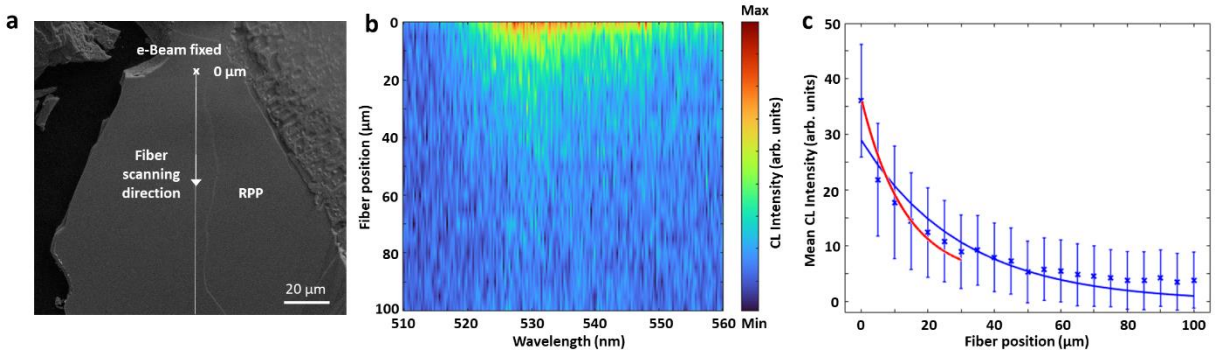

Supplementary Figure 4 | Fiber-collected cathodoluminescence (CL) spectroscopy of a pristine RPP flake. (a) Secondary electron SEM image of the investigated RPP flake. The electron beam is fixed at the position marked by the cross, while the fiber is scanned along the direction indicated by the white arrow. (b) CL spectra measured along the fiber scanning path shown in (a). (c) Mean peak intensity (with standard deviation) of the CL spectra from (b) plotted as a function of fiber position. The data are fitted to an exponential decay function of the form $\exp(-x/\gamma)$. The red line corresponds to a fit including the first seven data points, yielding a decay length of $\gamma = 13.2$ μm. The blue line shows the fit including all data points, resulting in a longer decay length of $\gamma = 30.3$ μm.

The energy-momentum map of the emitted CL has been measured using the mirror-collected CL spectroscopy system. The measured energy-momentum maps from the hBN-covered and uncovered regions of the hBN/RPP heterostructure (labeled as 1 and 2 in Supplementary Figure 5a) reveal nearly flat bands at the exciton energy of 2.4 eV (Supplementary Figure 5b, c). The presence of an excitonic flat band excludes any significant polaritonic or waveguiding behavior, which aligns with the proposed transport mechanism based on exciton-defect coupling in the hBN/RPP heterostructure. For comparison, the energy-momentum map of the pure hBN flake is also provided (Supplementary Figure 5d).

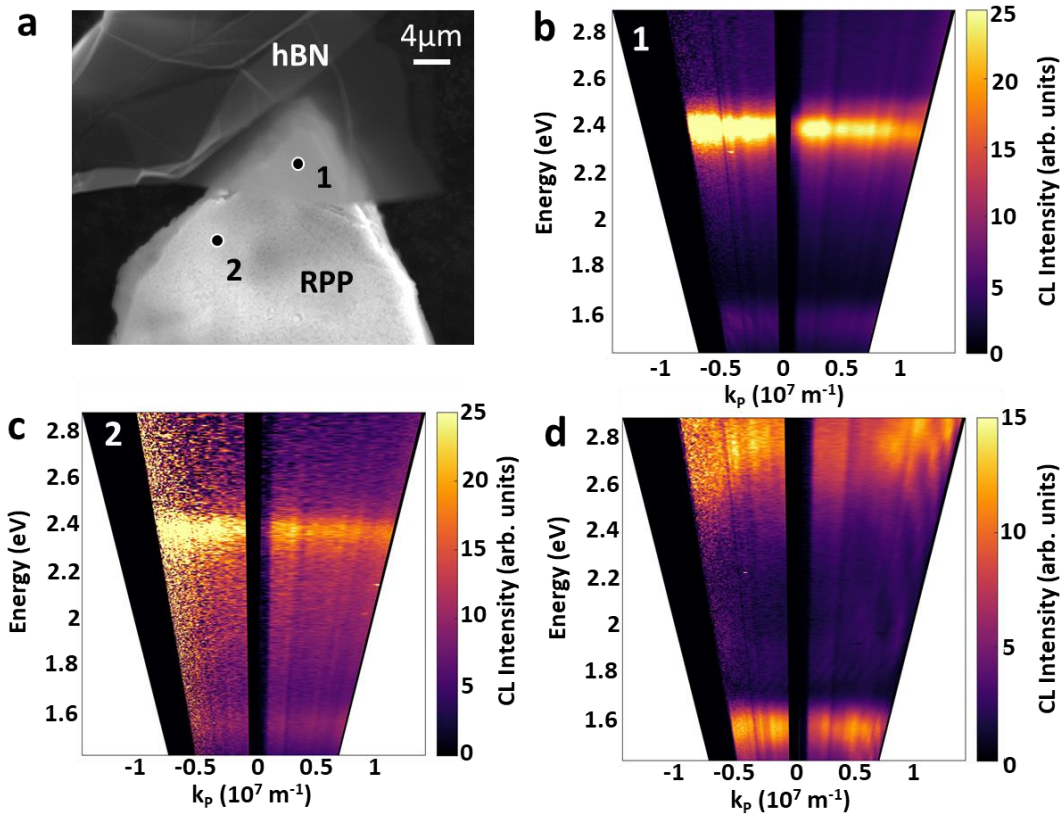

Supplementary Figure 5: The Energy-momentum map of the hBN/RPP heterostructures. (a) The secondary electron SEM image of the explored hBN/RPP structure. The energy-momentum map of the hBN/RPP heterostructures acquired at position 1 (b) and position 2 (c). The observed nearly flat band at the excitonic energy for the hBN/RPP heterostructure rejects polaritonic or waveguiding behavior and is in accordance with the proposed mechanism of coupled local defects. (d) Energy-momentum map of the pure hBN flake explored in Fig. 2(g), provided for the sake of comparison.

Supplementary Note 4: Monte Carlo Simulations.

In order to investigate the contribution of the secondary electrons and backscattered electrons of individual layers to the CL response, we perform depth-resolved electron energy-loss simulations using CASINO Software[1-3]. This approach has been proven to efficiently reproduce CL responses beyond Eikonal approximations, when combined with Maxwell's equations[4]. In this package, the elastic scattering events have been calculated using the tabulated Mott cross-sections, and the inelastic interactions have been approximated by the mean energy loss rate between the successive collisions, as described by the modified Bethe law by Joy and Luo[1]. The simulations employ a single-scattering model to track the electron trajectories and compute energy loss, expressed as $\Delta E = \frac{dE}{dx}.d$, where $\frac{dE}{dx}$ is the mean energy loss rate, and d is the distance between collisions[1,2]. Trajectory calculations terminate when electrons exit the sample, or their energy falls below a threshold value of 50 eV. For each scan point, the total deposited energy is calculated by summing energy loss contributions across the volume to generate energy-loss maps, revealing spatial distributions of energy absorption and scattering in the hBN/RPP heterostructures (Supplementary

Figure 6a to c). The energy deposition can also be analyzed as linear scans or cross-sectional views, providing insights into dynamic or static beam-sample interactions (Supplementary Figure 6d to f).

The electron beam is assumed to have a beam diameter of 10 nm, primary beam energy of 20 kV, and an incident electron number of 200,000. Cross-sectional views of energy-loss maps as a function of the electron beam position on a hBN/RPP heterostructure show the amount of the absorbed energy within the sample, scaling from black (no absorbed energy) to white (maximum absorbed energy) in Supplementary Figure 6a to c. As the penetrating electrons interact with the layers, they undergo both elastic and inelastic scatterings, resulting in their lateral and vertical trajectories as well as the generation of secondary electrons. When the electron beam impinges on the sample, 2000 nm away (on the left side) from the vacuum/RPP boundary, the electrons undergo significant energy loss in the top hBN layer and in the bottom carbon substrate (Supplementary Figure 6a).

For the case of electron beam impinging directly at the RPP edge, the electrons that penetrate the hBN/RPP region experience significant inelastic scatterings due to the underlying RPP layer in the right half (Supplementary Figure 6b). When the electron beam impinges 2000 nm away (right side) from the underlying vacuum/RPP boundary, a huge energy loss inside the RPP layer is observed (Supplementary Figure 6c). Better clarified by the linear scans, the maximum percentage of electron energy-loss occurs at a depth of approximately 3 μm in the bottom carbon tape when electron beam impinges the extruded part of the hBN layer (Supplementary Figure 6d), whereas the majority of energy dissipation occurs within the RPP layer at a depth of approximately 1 μm for excitation on the hBN/RPP heterostructure (Supplementary Figure 6e). Moreover, a higher portion of electron energy loss occurs in the hBN layer when the underlying RPP presents below it in the hBN/RPP heterostructure, which is due to the scattered electrons from the RPP back into the hBN. This observation can be the origin of the observed enhanced luminescent peaks at 635 nm and 800 nm in the hBN/RPP heterostructure with respect to extruded parts of hBN (Fig. 3a). As a clear confirmation, 2D simulation of the electron trajectories within the hBN/RPP heterostructure is presented in the inset of Supplementary Figure 6e, where red trajectories represent backscattered electrons and blue trajectories indicate absorbed electrons. Additionally, the fraction of secondary electrons captured in the RPP layer as a function of the electron beam impinging x-position is plotted in Supplementary Figure 6f, wherein the electron beam is scanned along x-axis over the RPP edge (at x=0 nm). As observed, the fraction of captured secondary electron in RPP that are responsible for the observed excitonic CL peak, increases with a sharp step-like transition at the RPP edge. Therefore, the simulated short-range trajectory of secondary electrons in the extruded part of the hBN layer (Supplementary Figure 6f) confirms that the observed CL signal, when the electron beam impacts the structure at locations far from the RPP flake, cannot be attributed to the excitation of RPP excitons by backscattered electrons.

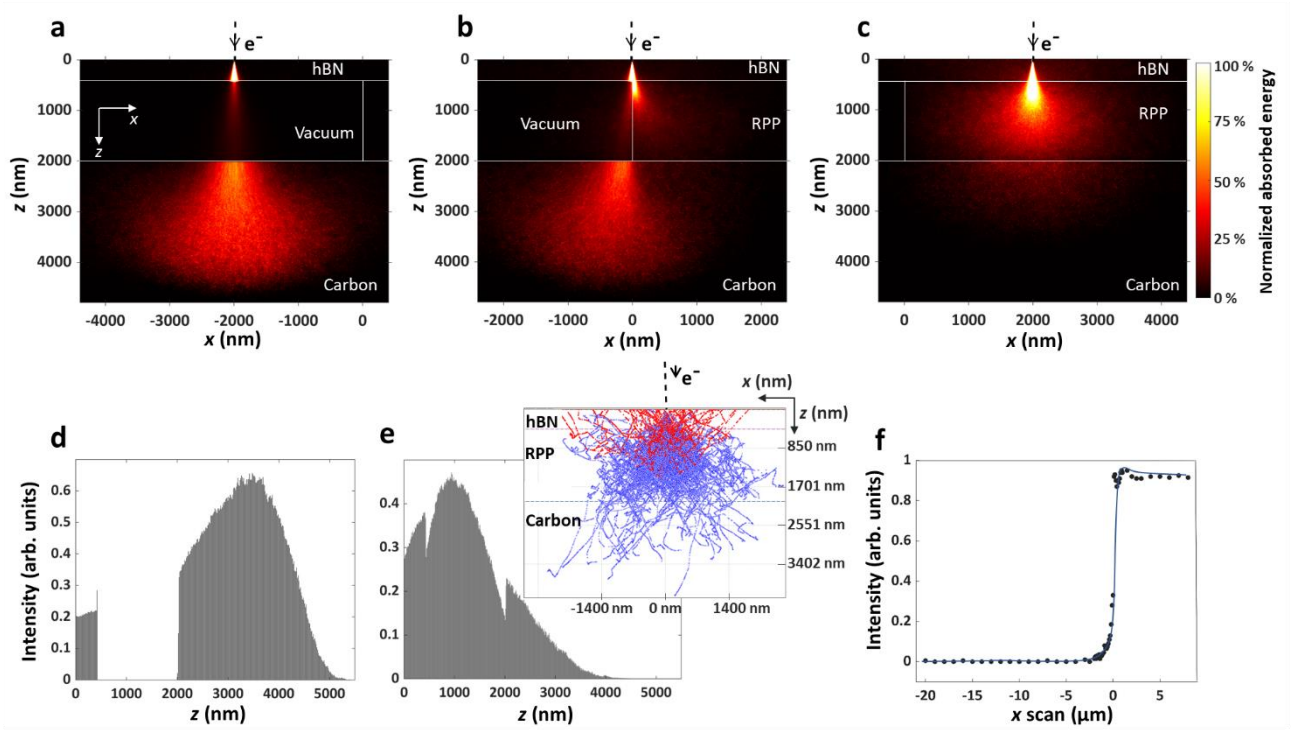

Supplementary Figure 6: Monte Carlo simulations of the spatial distribution of inelastically scattered electrons in the hBN/RPP heterostructure. Simulated energy-loss maps (480 × 480 points) are shown as a function of electron-beam scanning position on (a) a suspended hBN film over a carbon substrate at the distance of 2000 nm away from the RPP/vacuum interface, (b) the vacuum/RPP interface positioned on a carbon substrate, and (c) the hBN/RPP heterostructure at the distance of 2000 nm away from vacuum edge. Each map is generated with 200,000 incident electrons, and a beam diameter of 10 nm. Simulated electron energy-loss profiles for (d) the hBN/Vacuum/Carbon structure and (e) the hBN/RPP/Carbon structure. The inset illustrates electron trajectories of the secondary electrons (blue) and backscattered electrons (red) generated by a 20 kV electron beam. (f) Simulated secondary-electron fraction captured in RPP as a function of electron beam position from the RPP/vacuum edge.

Supplementary Note 5: The effect of RPP degradation on the optical response of the hBN/RPP heterostructure

The effect of RPP's inherent degradation on the CL characteristic of the hBN/RPP heterostructure is investigated by the mirror-collected CL spectroscopy technique. The secondary electron SEM image and the measured CL spectra of the freshly prepared hBN/RPP heterostructure are presented in Supplementary Figure 7a and b, and comparing it with the CL spectra of the same heterostructure after 30 days in Supplementary Figure 7c and d. The CL measurements are collected during moving the electron beam excitation spot along the blue arrows in parts a and c. The degraded underlying RPP experiences from a more significant electron charging effect and a reduced quality in the achieved secondary electron SEM image in Supplementary Figure 7c, as compared with Supplementary Figure 7a. Comparing the measured CL spectra in Supplementary Figure 7b and d reveals that the enhanced excitonic peak at 520 nm on the fresh hBN/RPP heterostructure diminishes to a very weak trace of excitonic peak in the degraded sample.

This evidence solidifies the proposed energy transfer between the excited luminescent defects in hBN and the excitons of RPP, leading to CL intensity ratio of I (520 nm)/I (800 nm) =2.64 for the fresh hBN/RPP heterostructure. However, the defined CL intensity ratio drops to 0.29 for the RPP-degraded heterostructure, which can be considered as a quantitative metric for the energy transfer from the hBN defects to the RPP excitons.

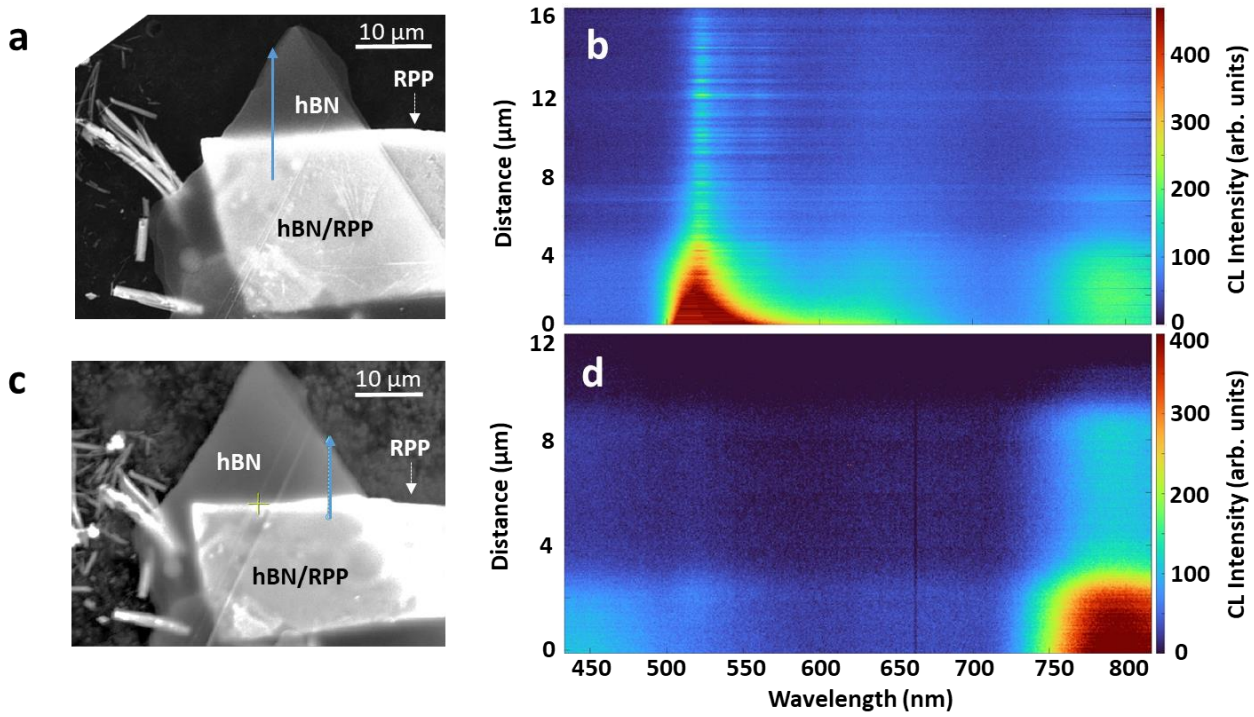

Supplementary Figure 7: Effect of one-month aging in RPP explored by the mirror-collected CL system. SEM image of (a) the prepared fresh hBN/RPP heterostructure, and (c) the same structure after one month, wherein blue arrows show the electron-beam scanning length. The measured CL spectra along the electron beam scanning length (b) for the fresh hBN/RPP sample, and (d) for the same hBN/RPP sample after one month.

References

1. Demers, H. *et al.* Three-dimensional electron microscopy simulation with the CASINO Monte Carlo software. *Scanning* **33**, 135–146 (2011).

2. Demers, H., Poirier-Demers, N., Phillips, M. R., de Jonge, N. & Drouin, D. Three-Dimensional Electron Energy Deposition Modeling of Cathodoluminescence Emission near Threading Dislocations in GaN and Electron-Beam Lithography Exposure Parameters for a PMMA Resist. *Microscopy and Microanalysis* **18**, 1220–1228 (2012).

3. Drouin, D. *et al.* CASINO V2.42—A Fast and Easy-to-use Modeling Tool for Scanning Electron Microscopy and Microanalysis Users. *Scanning* **29**, 92–101 (2007).

4. Chahshouri, F., Taleb, M., Diekmann, F. K., Rossnagel K., Talebi, N. Interaction of excitons with Cherenkov radiation in WSe2 beyond the non-recoil approximation, *Journal of Physics D: Applied Physics* **55** (14), 145101 (2022).